Geophys. J. Int. (2005) **163,** 152–164 doi: 10.1111/j.1365-246X.2005.02703.x

High-resolution imaging of the Bear Valley section of the San Andreas fault at seismogenic depths with fault-zone head waves and relocated seismicity

Jeff McGuire[1] and Yehuda Ben-Zion[2]

[1]*Department of Geology and Geophysics, Woods Hole Oceanographic Institution, Woods Hole, MA,* 02543, *USA*
[2]*Department of Earth Sciences, University of Southern California, Los Angeles, CA,* 90089-0740, *USA*

Accepted 2005 June 1. Received 2005 March 3; in original form 2004 June 29

SUMMARY

Detailed imaging of fault-zone (FZ) material properties at seismogenic depths is a difficult seismological problem owing to the short length scales of the structural features. Seismic energy trapped within a low-velocity damage zone has been utilized to image the fault core at shallow depths, but these phases appear to lack sensitivity to structure in the depth range where earthquakes nucleate. Major faults that juxtapose rocks of significantly different elastic properties generate a related phase termed a fault-zone head wave (FZHW) that spends the majority of its path refracting along the fault. We utilize data from a dense temporary array of seismometers in the Bear Valley region of the San Andreas Fault to demonstrate that head waves have sensitivity to FZ structure throughout the seismogenic zone. Measured differential arrival times between the head waves and direct *P* arrivals and waveform modelling of these phases provide high-resolution information on the velocity contrast across the fault. The obtained values document along-strike, fault-normal, and downdip variations in the strength of the velocity contrast, ranging from 20 to 50 per cent depending on the regions being averaged by the ray paths. The complexity of the FZ waveforms increases dramatically in a region of the fault that has two active strands producing two separate bands of seismicity. Synthetic waveform calculations indicate that geological observations of the thickness and rock-type of the layer between the two strands are valid also for the subsurface structure of the fault. The results show that joint analysis of FZHWs and direct *P* arrivals can resolve important small-scale elements of the FZ structure at seismogenic depths. Detailed characterization of material contrasts across faults and their relation to earthquake ruptures is necessary for evaluating theoretical predictions of the effects that these structures have on rupture propagation.

Key words: fault models, head waves, interfaces, relocated seismicity, traveltimes, waveform modelling.

1 INTRODUCTION

Crustal faults are typically associated at the surface with a damage zone comprised of highly fractured rock, but their structure at seismogenic depths is very difficult to resolve. Determining the physical properties of the zone in which ruptures occur is a fundamental starting point for developing realistic mechanical models of the earthquake process. Moreover, these material properties are a natural target for long-term monitoring because many physical models include spatio-temporal variations in the composition and strength of the fault-zone (FZ) structure (Sibson 1977; Dieterich 1979; Blanpied *et al.* 1992; Marone *et al.* 1995; Massonnet & Vadon 1996; Andrews & Ben-Zion 1997; Lyakhovsky *et al.* 2001; Scholz 2002). The characterization of *in situ* FZ properties at seismogenic depths lags significantly behind theoretical and laboratory studies, and there is considerable uncertainty even in basic issues such as the width of the shear zone of major faults at seismogenic depths. The surface expression of a single earthquake rupture can be as wide as 50–500 m (Johnson *et al.* 1997), but the zones that accommodate long-term slip in exhumed portions of the San Gabriel and Punchbowl FZs in California are only a few centimetres wide (Chester & Chester 1998; Evans & Chester 1995). Gravity, electromagnetic, seismic reflection/refraction and geodetic studies reveal broad (order kilometer wide) low-velocity zones around faults that result from the cumulative damage caused by repeated ruptures on geological timescales (Stierman 1984; Eberhart-Phillips *et al.* 1995; Fialko *et al.* 2002). However, the depth extent of these broad damage zones is poorly resolved. Body wave tomography studies have also imaged kilometre-wide regions of low seismic velocity with apparently elevated fluid content (Eberhart-Phillips *et al.* 1995; Thurber

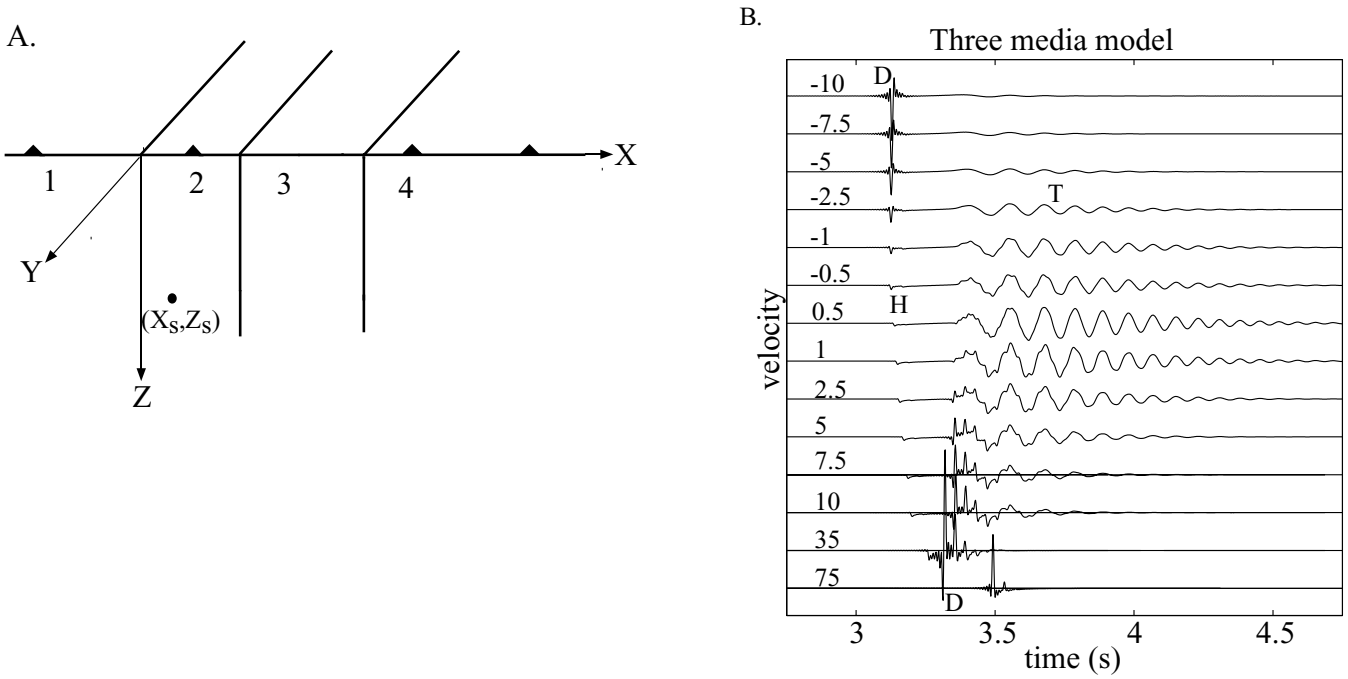

Figure 1. A model of FZ structure that is utilized in the waveform fitting section of the paper and corresponding examples of synthetic velocity seismograms with head, body and trapped waves based on the solution of Ben-Zion & Aki (1990) and Ben-Zion (1998). (A) The model has two vertical elastic layers with width W_i between two elastic quarter spaces. The media material properties are density (ρ_i), shear modulus (μ_i), wave speed (c_i) and quality factor (Q_i). The layers are referred to by name and index (numerical labels in the figure) as: the fast (1) and slow (4) quarter spaces, a transition layer (2) and a core FZ layer (3). An SH line dislocation (solid circle) is located in medium 2. (B) Synthetic velocity seismograms for a single low-velocity FZ layer with width W_2 between a fast and slow quarter space at receivers along the free surface with horizontal x coordinates in units of W_2. Direct (D), Head (H), and Trapped (T) waves are labelled. The stations located within the slow quarter space and relatively close to the fault ($0 < x < 10$) begin with nearly nodal head waves that are followed by opposite polarity, large-amplitude direct waves. This diagnostic signature is easily identified on seismograms from the Bear Valley section of the SAF. Modified from Ben-Zion (1998).

et al. 1997). However, these zones are probably blurred versions of the true structures. Since the above imaging studies use signals with relatively long wavelengths, or waves that spend only a small percentage of their path in the FZ, they offer little hope of characterizing the narrow mechanical structure at seismogenic depths that was (will be) involved in the last (next) rupture.

Beginning about 15 yr ago, it appeared that seismic phases associated directly with low-velocity layers of damaged rock in FZ structures would provide possibilities for characterizing these zones (Ben-Zion & Aki 1990; Ben-Zion & Malin 1991; Li & Leary 1990; Li *et al.* 1994). A coherent FZ layer with low-velocity damaged rock is expected (Fig. 1) to act as a waveguide by trapping reflected seismic energy within the layers that separate the two surrounding crustal blocks. Such FZ trapped waves are analogous to Love waves in a horizontal low-velocity layer and they have been recorded at numerous faults from both explosion and natural earthquake sources. Modelling these recordings indicated in several places the presence of FZ layers with width ranging from tens to hundreds of metres, strong reduction of seismic velocity and strong attenuation (e.g. Li *et al.* 1994a,b, 1997; Hough *et al.* 1994; Nishigami *et al.* 2001; Haberland *et al.* 2003). In addition, Li *et al.* (1998) found a time dependence of these FZ properties following the Landers rupture that was consistent with an expected post-seismic fault re-strengthening (Dieterich 1979; Marone 1998; Scholz 2002). While the existence of these trapped waves is easily observable on appropriate seismograms, constraining the depth extent of the trapping FZ layer has been difficult.

A recent series of observational studies concluded that the low-velocity FZ waveguides that produce trapped waves at the San Andreas, Landers, San Jacinto and North Anatolian faults are generally limited to the upper ∼3–4 km of the crust (Ben-Zion *et al.* 2003; Korneev *et al.* 2003; Michael & Ben-Zion 1998; Peng *et al.* 2003; Lewis *et al.* 2005). Igel *et al.* (2002), Jahnke *et al.* (2002) and Fohrmann *et al.* (2004) showed with 3-D wave-propagation calculations that sources well outside and below shallow FZ layers can produce ample trapped wave energy at stations close to the FZ. In contrast, the generation of trapped waves in a low-velocity FZ layer that is continuous with depth requires sources that are inside or very close to the low-velocity structure (Ben-Zion & Aki 1990; Jahnke *et al.* 2002). Many events located well outside the Karadere–Duzce section of the North Anatolian Fault generate considerable trapped wave energy (Ben-Zion *et al.* 2003) and similar results were obtained for the Landers rupture zone and the San Jacinto fault (Peng *et al.* 2003; Lewis *et al.* 2005). It is possible that slivers of damaged FZ rock extend at places to seismogenic depths. However, the observations of FZ trapped waves due to sources well outside the fault imply that the trapping structures are overall limited to the stable (velocity strengthening) uppermost portion of the crust that is above the seismicity and largely mechanically passive. Shallow trapping structures were also found for faults in central Italy (Rovelli *et al.* 2002) and central Japan (Mamada *et al.* 2004). The results imply that FZ trapped waves are generally not useful for *in situ* characterization of FZ structure in the depth range where earthquakes nucleate and the majority of co-seismic slip occurs (3–15 km). Imaging this

highly important and potentially very narrow region remains an unsolved observational challenge.

Another characteristic feature of major crustal faults is that they often have accumulated a large enough offset that the rock types in the two bounding crustal blocks have significantly different material properties. This is true over much of the length of the San Andreas Fault (SAF) where these broad differences have been imaged by local tomographic studies in the Bear Valley (Thurber *et al.* 1997) and Parkfield sections (Michelini & McEvilly 1991; Eberhart-Phillips & Michael 1993; Lees & Malin 1990) of the fault. The contrast is also present in more regional images of the Big Bend portion of the SAF where the velocity contrast may extend into the uppermost mantle (Fuis *et al.* 2001; Tanimoto & Sheldrake 2002). Seismic energy generated near such a sharp contrast in rock types will refract along the interface (Ben-Zion 1989; Ben-Zion & Aki 1990) in a manner analogous to head wave refractions along horizontal interfaces in the earth, such as the Moho discontinuity (i.e. *Pn*). Fault zone head waves (FZHWs) generated by slip along material interfaces are the first arriving seismic phases at near-fault stations on the slower side of the fault and are characterized by an emergent waveform with opposite polarity from that of the following body wave. McNally & McEvilly (1977) discussed distortions of focal mechanisms due to first-arriving opposite-polarity head waves along the Bear Valley section of the SAF. Ben-Zion & Malin (1991) and Ben-Zion *et al.* (1992) performed traveltime analysis of FZHWs and direct body waves in the Parkfield section of the SAF. Since FZHWs spend almost their entire path between source and receiver along the fault interface, imaging methods based on these phases should be able to provide high-resolution information on FZ structure at seismogenic depths. In this paper, we systematically analyse a data set of FZ head and *P* waveforms generated by earthquakes in the Bear Valley section of the SAF together with accurate hypocenter locations. The observations show that a sharp material interface along the SAF extends through the seismogenic zone in the study area. Our analysis demonstrates the ability of FZHWs to image important structural elements of large faults at seismogenic depths.

The existence of sharp material interfaces in the structure of the SAF at depth has significant implications for earthquake dynamics, since rupture along material interface produces a change of normal stress that is proportional to the spatial derivative of in-plane slip (Weertman 1980; Adams 1995; Andrews & Ben-Zion 1997). The interaction between slip and normal stress along a material interface can reduce dynamically the frictional strength—potentially to zero—making material interfaces mechanically favored surfaces for rupture propagation (Ben-Zion 2001). Analytical and numerical models have shown that rupture along a fault that separates different media can occur as a narrow wrinkle-like pulse that propagates predominately in the direction of slip in the more compliant medium (Weertman 1980; Adams 1995; Andrews & Ben-Zion 1997; Ben-Zion & Huang 2002; Cochard & Rice 2000; Ranjith & Rice 2001). Characteristic features of the wrinkle-like pulse include: (1) strong correlation between variations of normal stress and slip, (2) strongly asymmetric motion across the fault (3) self-sharpening with propagation distance and (4) preferred direction of rupture propagation. Anooshehpoor & Brune (1999) observed features (1)–(4) of the wrinkle-like rupture in laboratory experiments of sliding along a material interface. These features were also present in the early sliding experiments of Schallamach (1971). If these properties characterize ruptures on natural faults, they would have fundamental consequences for many aspects of earthquake physics, including effective constitutive laws, suppression of branching, the heat flow paradox, short rise-time of earthquake slip and expected seismic shaking hazard (Ben-Zion & Andrews 1998; Ben-Zion 2001). A necessary first step towards determining the importance of the wrinkle-like pulse effects is a detailed characterization of a FZ that juxtapose rocks of significantly different elastic properties.

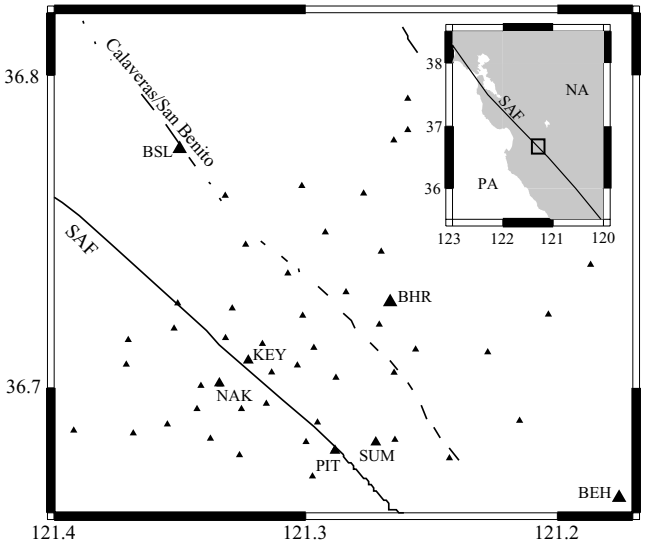

Figure 2. Seismic stations (triangles) along and around the Bear Valley section of the SAF (solid line). The triangles labelled KEY and SUM show locations of the temporary 1994–1995 seismic stations mentioned in the text. The large labelled triangles (BSL, BHR, BEH) are stations of the NCSN mentioned in the text. The Calaveras/San-Benito fault is shown as a dashed line. The inset shows the position of the Bear Valley region (box) on a large-scale map of the Pacific (PA)—North America (NA) plate boundary.

2 THE BEAR VALLEY SECTION OF THE SAN ANDREAS FAULT

The Bear Valley region of the SAF, in the northern end of the creeping section (Fig. 2), generates complex wave-propagation effects resulting from the local FZ structure. The fault is bounded on the southwest side by granitic and Miocene volcanic rocks of the Gabilan range. On the northeast side there is a 4- to 10-km wide FZ system between the SAF and the subparallel Calaveras fault, consisting of Pliocene age sedimentary units with isolated slivers of granite, Mesozoic intrusive rocks, Miocene volcanic rocks and Cretaceous sedimentary rocks (Thurber *et al.* 1997; Li *et al.* 1997). Thus, the SAF in this region is a boundary between high-velocity materials on the SW side (*P* velocity >5 km s^{-1}) and low-velocity material on the NE side (*P* velocity <4 km s^{-1}). This boundary has been imaged by a number of active and passive source seismology studies (Stewart 1968; Thurber *et al.* 1997; Walter & Mooney 1982). The material contrast is strong enough to generate significant head waves that are recorded as the first arrivals at stations near the fault on the NE side (McNally & McEvilly 1977).

The normal distance on the slower side of the fault for head wave first arrivals is $x_c = r \tan[\cos^{-1}(\alpha_2/\alpha_1)]$, where r is the travelled distance along the fault and α_1, α_2 are the average *P* wave velocities on the slower and faster sides, respectively (Ben-Zion 1989). Fig. 3 shows examples of head and direct body waves recorded by NCSN station BHR about 5 km from the fault. Only events with distance greater than $\sim$6 km from the station (in the along-strike direction) show head waves as the first arrival, as would be expected for about a 30 per cent velocity contrast. This estimate is roughly consistent

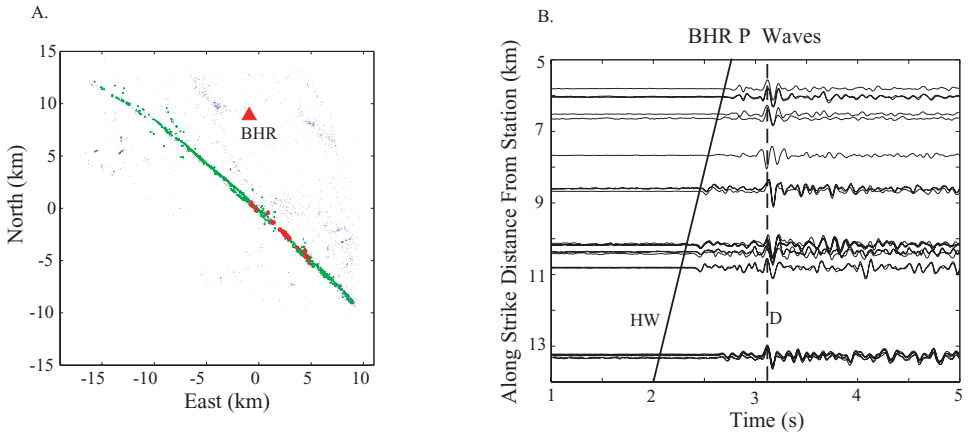

Figure 3. Examples of head wave recordings at NCSN station BHR. (A) The locations of earthquakes that generated *P* waveforms with (red) and without (green) clear first arriving head waves at BHR. Blue dots indicate the locations of other relocated background seismicity. The head waves arrive first only for events with sufficient propagation distance along the fault. (B) Vertical component *P* waveforms for the events plotted with red in A. The seismograms have been aligned on the first peak of the direct (D) arrival (dashed line). An opposite polarity, low amplitude head wave (HW) arrival is seen before the direct wave. The moveout of the head waves is shown approximately by the solid line. Head wave first arrivals are seen at station BHR only for events in a relatively limited portion of the fault owing to the large (5 km) distance of the station from the fault.

with the tomography study of Thurber *et al.* (1997). Other nearby NCSN stations, such as BEH and BSL, do not show clear first arriving headwaves. This indicates that the velocity contrast is strongest along the paths to BHR and that stations closer than 5 km from the fault are necessary to study the head waves in detail.

The wrinkle-like slip pulse hypothesis would be consistent with a preference for rupture propagation to the SE in the Bear Valley section of the SAF owing to the strong, ∼25–30 per cent, velocity contrast across the fault. Given the existing structure and sense of loading, the theory predicts (e.g. Weertman 1980; Ben-Zion 2001) a dynamic weakening at a propagating rupture tip to the SE and dynamic strengthening to the NW. Rubin (2002) and Rubin & Gillard (2000) relocated earthquakes in the NCSN catalogue between 1984 and 1997 along this portion of the fault, and found that more than twice as many immediate aftershocks occurred to the NW of the mainshock as to the SE. They interpreted this asymmetry as being consistent with the wrinkle-like slip pulse mechanism, because if ruptures propagate primarily to the SE with dynamic weakening (as predicted) then the barriers that stopped them are stronger in this direction than those immediately NW of the rupture area. These studies conclude that even very small ruptures (of events with magnitude 1–2) are sensitive to the velocity contrast across the fault, implying that the damage zone is very thin at seismogenic depths.

3 LOCAL ARRAY DATA

A 48-station PASSCAL array (Fig. 2) was deployed for 6 months in this region during 1994 and 1995 by Thurber *et al.* (1997). The instruments were a mix of standard short period seismometers, primarily Mark Products L22s, L4s and Teledyne S-13s, and covered both sides of the SAF with the closest stations within about 300 m of the surface trace. In general, *P*- and *S*-wave recordings on the SW side of the fault are very impulsive with much higher frequency content than recordings on the NE side of the fault, owing to the across fault contrast in rock type. Similar observations characterize seismic records on the opposite sides of the SAF at Parkfield (Ben-Zion & Malin 1991). The station geometry was designed primarily for direct wave tomographic imaging of the variations in elastic structure and to determine the dip of the fault. Nevertheless,

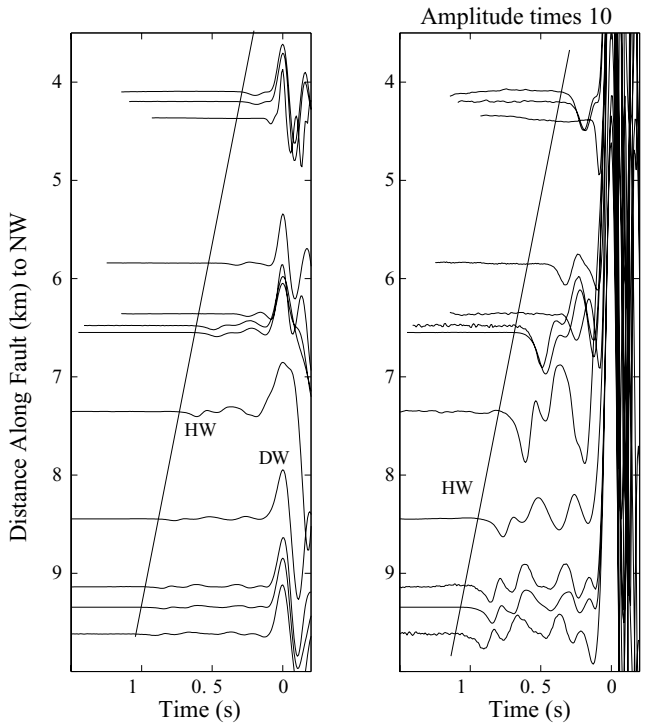

Figure 4. Head waveforms recorded by the temporary station SUM located approximately 2 km from the SAF. The earthquakes were located to the NW of SUM at various depths. Left: *P*-wave recordings aligned on the peak of the first swing of the direct arrival. The moveout of the head waves is shown approximately by the solid line. Right: The same recordings and alignment as in the left-hand panel, but the scale has been multiplied by ten. The head wave arrivals have the opposite polarity of the direct *P* waves.

this data set provides excellent evidence for head wave propagation along a 15-km section of the SAF. Fig. 4 shows waveforms from earthquakes that generated first arrival head waves at station (SUM) located only 1–2 km from the fault on the NE side. The waveforms begin with a low amplitude first arrival having an opposite polarity to the later arriving direct wave. This near nodal head wave

amplitude is a consequence of the (strike-slip) *P*-wave radiation pattern (Ben-Zion 1989, 1990).

The head wave arrivals were observed on all three types of sensors, as would be expected given that they contain significant energy in the 5- to 25-Hz band, well above the (variable) lower corner frequency of each instrument. The head wave arrivals are ubiquitous at the stations on the NE side of the fault. However, the differential time picking error is minimized for stations about 1–2 km from the fault owing to simpler waveform shapes than stations closer to the fault and larger differential times than those observed further from the fault. The stations immediately adjacent to the fault, such as PIT (Fig. 2), have significantly more complicated waveforms that make picking the various arrivals more ambiguous. In this study, we focus on head waveforms from two of the stations located in the ∼1- to 2-km distance range from the fault, SUM and KEY (Fig. 2). These stations recorded some of the best data sets for our purposes in terms of the distribution of the generating events (i.e. no data gaps) and unambiguous waveforms with large direct minus head wave differential arrival times. Additional information about the fine structure of the FZ appears to be present in the complicated waveform shape of the head wave arrival. The Bear Valley data set provides an opportunity to utilize this type of waveform information. The relatively large delay time between the head and direct wave arrivals allows a longer and more complex head waveform to be analysed than for similar head waves at Parkfield.

4 RESULTS

4.1 Earthquake relocation

To extract as much information as possible from the PASSCAL head-waveform data set requires accurate knowledge of the relative and absolute positions of the earthquake sources that generated the waveforms. Since only about 200 earthquakes were sufficiently recorded for earthquake locations during the 6-month deployment (Thurber *et al.* 1997), it is necessary to use additional (longer) data sets to illuminate details of FZ structures in this region. Most of the seismicity in the area covered by the temporary array was not relocated by Rubin & Gillard (2000). To image the seismogenic structures in the study area we relocated 6700 earthquakes recorded by 140 Northern California Seismic Network (NCSN) stations between

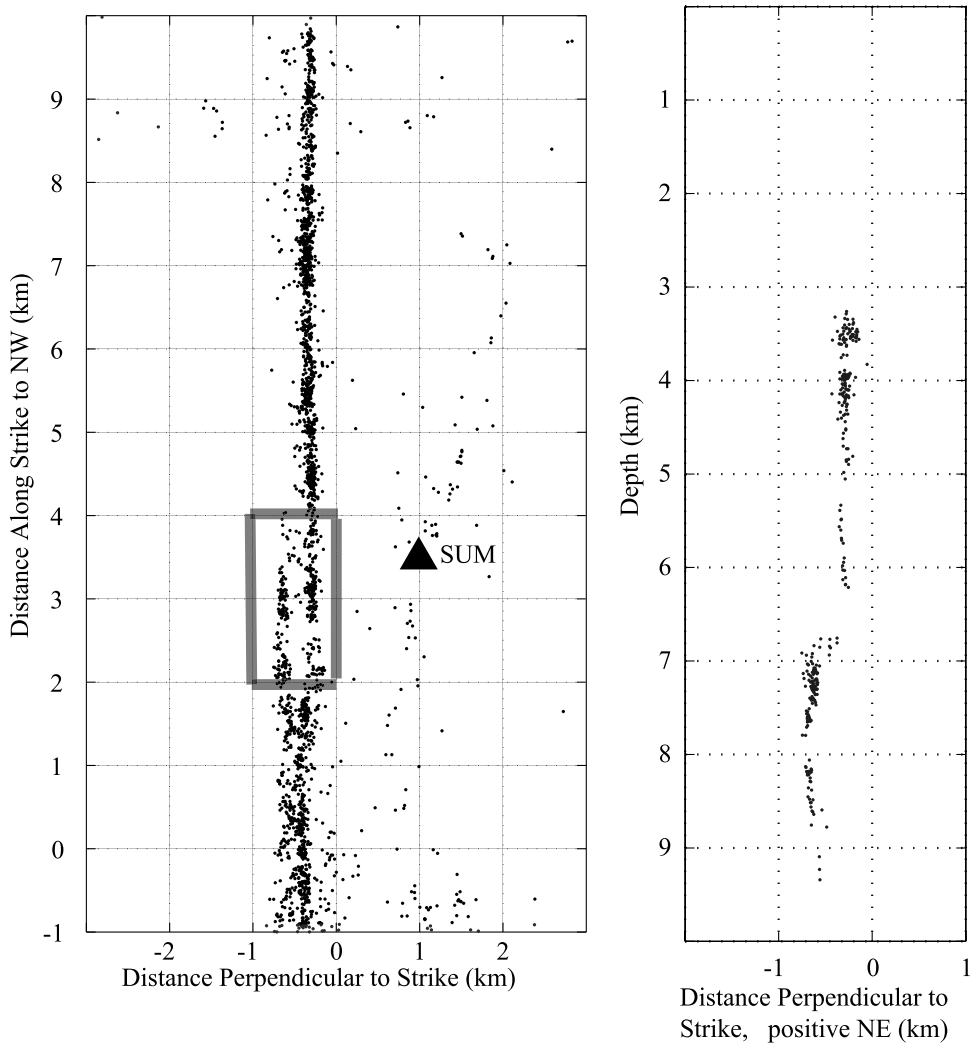

Figure 5. Relocated earthquake positions exhibiting a transition in the structural complexity of the SAF. (A) A map view of the seismicity in the vicinity of station SUM (triangle). The box denotes the region of seismicity shown in a vertical cross-section in B. (B) A vertical cross-section of seismicity in the region SE of SUM that shows two active strands in map view.

1990 and 2002. The relocation analysis used the double-difference technique of Waldhauser & Ellsworth (2000) and *P*- and *S*-wave differential arrival times taken from the NCSN catalogue picks. The employed velocity model was the standard 7-layer V_p model for Northern California (Schaff *et al.* 2002; Waldhauser & Ellsworth 2000), which does not account for the velocity contrast across the fault. The LSQR implementation (Paige & Saunders 1982) of the double-difference algorithm was used. Arrival times from the temporary deployment were not used owing to the small percentage of the data set for which they were available.

The vast majority of the relocated seismicity collapses onto a well defined tabular structure (Fig. 5) that is typically about 100–200-m wide, probably reflecting the uncertainty in the relative locations derived from catalogue arrival time picks. While this uncertainty could be improved by the incorporation of waveform-derived (cross-correlation) measurements of the relative arrival times, it is sufficient for our purposes. A 200-m uncertainty in the relative location of two earthquakes corresponds to an uncertainty of about .01 *S* in their predicted head wave minus direct wave differential travel time, or about 2 per cent of a typical measurement. The error induced by the uncertainty in relative locations is at least a factor of two smaller than the uncertainty in the picking of the differential times. The absolute location of the seismicity is more uncertain than the relative locations between earthquakes owing to the strong lateral velocity variations.

A long-standing debate exists over whether the seismicity in this region is offset to the SW of the surface trace of the SAF as a result of a significant fault dip (Aki & Lee 1976), or if the seismicity resides on a near-vertical plane under the fault trace and the apparent offset is an artifact of the velocity heterogeneity (e.g. Bakun *et al.* 1980; Ellsworth 1975). More recently, a joint tomographic and earthquake location inversion by Thurber *et al.* (1997) concluded that the fault dipped at 70° to the SW, causing the earthquakes to be offset about 2 km from the surface trace. Since our relative locations indicate a near-vertical fault, we shifted the results of the double-difference locations 0.7-km to the NE for plotting purposes to account for the likely bias from the velocity contrast. The 0.7-km shift was chosen so that the near-vertical plane of seismicity is located about 100–200 m SW of the station PIT, which is approximately this distance from the surface trace of the SAF (C. Thurber, personal comm., 2001). Additionally, a shift of approximately this magnitude was necessary to produce polarities (and frequency content) consistent with right lateral focal mechanisms from a vertical fault at stations close to the fault on the SW side such as NAK. The uncertainty in the absolute locations is in the direction normal to the fault, so it has only a minimal effect on the analysis of differential traveltimes in Section 4.2 because those measurements are related to the distance travelled along the fault. However, the uncertainty in the absolute locations has an effect on the relative amplitude of the head and direct waves produced by the waveform simulations in the subsequent Section 4.3.

One dramatic feature of the relocated seismicity is the visible transition from a single fault strand that is active throughout the seismogenic depth range (3–9 km) in the region northwest of station SUM, to a pair of active parallel strands SE of this station (Fig. 5). The two strands are active in different depth ranges, with the SW strand generating earthquakes in the 7- to 9-km depth range and the NE strand being active in the 3- to 6-km depth range. The relative shift of the deeper events to the SW does not appear to be an artefact of the overall velocity contrast, as the velocity contrast is strong in both the one- and two-strand areas (see Section 4.2). The structural transition is also manifested clearly by the complexity of waveforms generated by events in the one- and two-strand regions (Section 4.3). Moreover, the transition of the fault from one strand to two in the vicinity of SUM has been mapped in the surface geology (Dibblee 1974). The SAF in this region separates overall granitic rocks on the SW from Quaternary sediments to the NE, but in the vicinity of SUM the two mapped traces of the fault are separated by a sliver of granitic rocks that is a few hundred m thick. The mapped geology agrees well with the earthquake relocations both in terms of the spatial location of the transition and also in the separation distance which is about 300–400 m in the earthquake locations. The long-standing uncertainty on whether the earthquakes in this region are offset to the SW of the surface trace may result in part from the presence of multiple active (near-vertical?) fault strands in a section of the study area, and possibly the miss-association of head wave first arrival time picks with direct wave ray paths.

4.2 Geometrical analysis of head wave arrivals

Differential arrival times between the head and direct waves demonstrate that: (1) the material interface corresponds to a *P*-wave velocity contrast of at least 20 per cent, (2) the contrast occurs as a very sharp transition (<1 km) and (3) it extends throughout the seismogenic zone. Ben-Zion & Malin (1991) noted that for an interface between two different quarter spaces, the differential arrival time (Δt) grows with distance (r) traveled along the fault as $\Delta t \sim r(\Delta\alpha/\alpha^2)$, where α and $\Delta\alpha$ are the average and differential *P*-wave velocities, respectively. Therefore if the average *P*-wave velocity is known, the slope of a differential arrival time versus propagation distance curve can be used to estimate the strength of the velocity contrast $\Delta\alpha/\alpha$. The differential time depends on the total distance traveled along the fault and is expected to grow with distance from the source to the station in both the along-strike and up-dip directions. Fig. 6 demonstrates the increase in differential traveltime for up-dip propagation using a set of earthquakes that occurred almost directly under SUM. Owing to the negligible portion of their propagation path in the along-strike direction, the differences between the seismograms generated 3 and 7 km below SUM provide a clear demonstration of the strength of the velocity contrast in the seismogenic zone, and the sensitivity of head waveforms to that structure. The shallow and deep events generated direct *P* waves that are preceded by opposite polarity head waves arriving 0.2 and 0.4 s earlier, respectively. This moveout with up-dip propagation distance (roughly 0.04 s km^{-1}) requires that a strong (∼20 per cent) velocity contrast exists throughout the seismogenic zone.

To constrain the strength of the velocity contrast and its sharpness, we picked differential arrival times for earthquakes recorded at stations SUM and KEY from events located both within and to the southeast of the array. Owing to the distribution of the seismicity during the 6-month deployment, much of the highest quality head wave data is generated by earthquakes located 5–10 km to the southeast of the array. Numerous earthquakes also occurred within the array but relatively little seismicity occurred to the northwest. Thus, we focus on three profiles of head wave seismograms that utilize the available seismicity distribution to demonstrate the sensitivity of direct minus head wave arrival times to both the along-strike and fault-normal variations in elastic properties. Station SUM recorded head waves from earthquakes located in the opposite along-strike directions (Fig. 7). To measure the differential traveltimes, the seismograms from a series of earthquakes in a particular direction (and distance range) were aligned on the peak of the first swing of the direct wave. The head wave arrival time was then picked by hand on

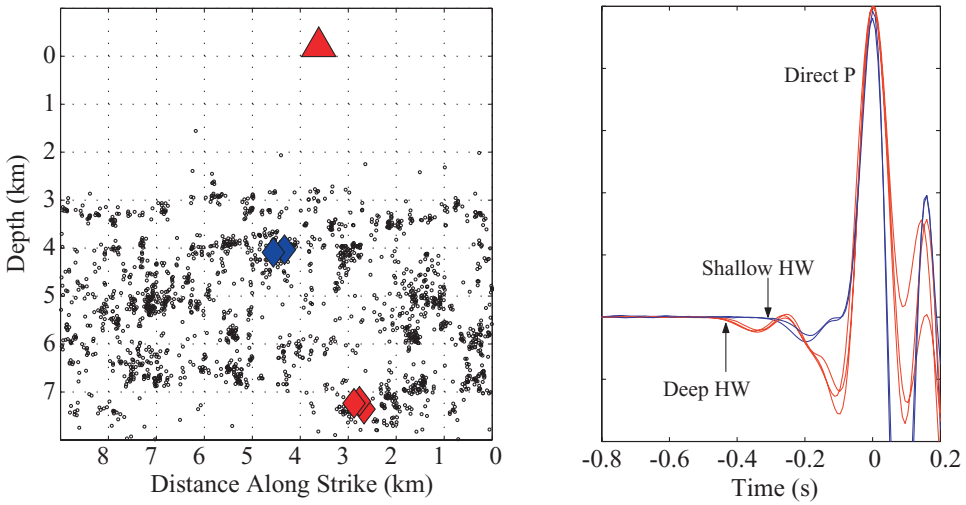

Figure 6. Example seismograms illustrating the depth dependence of head wave moveout at station SUM (triangle). Left: A cross-section of earthquake relocations in the vicinity of SUM. Two clusters of seismicity recorded by SUM are indicated by blue (shallow) and red (deep) diamonds. Right: A comparison of the *P*-wave recordings from the shallow (blue lines) and deep (red lines) clusters. Since there is a negligible difference in the along-strike propagation distance for the two clusters, the increased moveout of the head waves from the deep events requires that the velocity contrast extends throughout the seismogenic zone.

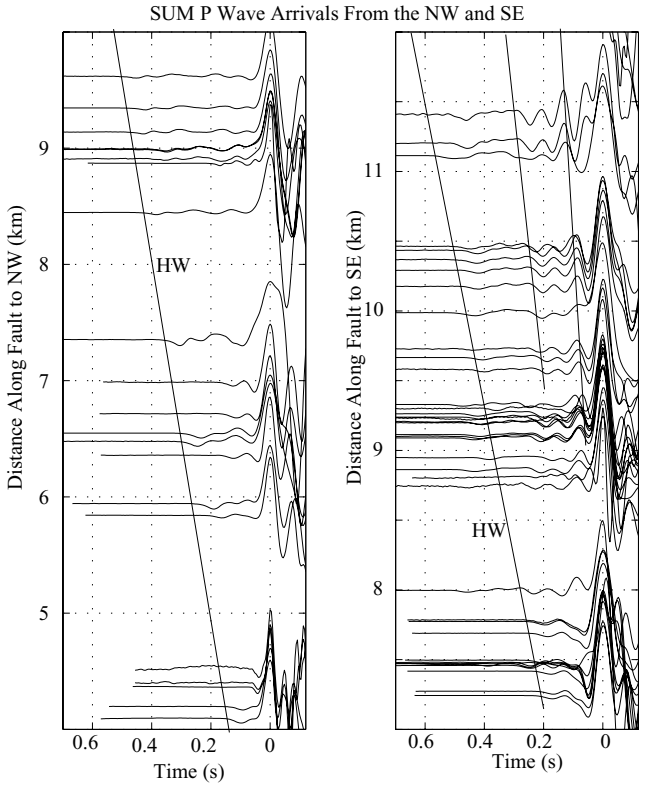

Figure 7. Comparison of vertical-component *P* waveforms recorded at station SUM for earthquakes in the opposite directions along strike. Arrivals from the SE are flipped to match the polarities from the NW and the waveforms are aligned on the first swing of the direct wave. The waveforms from the NW are relatively simple while those from the SE have additional arrivals.

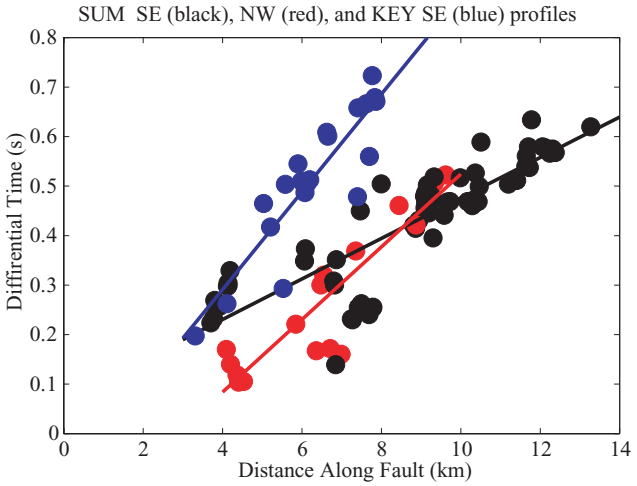

Figure 8. Differential traveltime picks for earthquakes to the SE (black) and NW (red) of station SUM, along with events to the SE of station KEY (blue). The lines are least-squares fits and their slopes (given in the text) provide estimates for the velocity contrast for the imaged section of the fault.

each recording. The differential arrival time picks (Fig. 8) show that the moveout of the head wave relative to the direct wave is faster for earthquakes occurring to the NW of SUM (.07 s km^{-1}) than for those to the SE (.04 s km^{-1}). This difference may result from the greater average source depth of the events to the SE of SUM, suggesting that the magnitude of the velocity contrast is greatest in the 0- to 3-km depth range sampled by the majority of earthquakes NW of SUM. The slopes of the differential time moveout curves, combined with an average *P*-wave velocity of about 5.0 km s^{-1}, indicate velocity contrasts ($\Delta\alpha/\alpha$) over the depth range of the employed earthquakes of 20 per cent SE of SUM and 35 per cent NW of SUM. The 35 per cent contrast corresponds to the region in the center of the temporary array and is in good agreement with the *P*-wave velocity estimates over the 1- to 5-km depth range in the tomographic image of Thurber *et al.* (1997).

Station SUM is located about 1 km from the surface trace of the SAF. If the FZ at depth is thinner than 1 km, differential times at SUM would average over some material outside the FZ proper and lead to an underestimate the *P* wave speed decrease within the FZ. Station KEY is within about 300 m of the surface trace of the SAF (C. Thurber, personal communication, 2001), and shows clear head

wave recordings from earthquakes located to its SE (i.e. the events used in the NW profile for SUM). The differential times at KEY have (Fig. 8) a moveout of 0.10 s km^{-1}, which corresponds to a $\Delta\alpha/\alpha$ of about 50 per cent. Owing to the proximity of KEY to the surface trace, a 50 per cent contrast is probably a more accurate estimate of the average velocity reduction within the FZ itself (i.e. approximately 3.0 km s^{-1}). Taken together, the three profiles of Fig. 8 demonstrate that the magnitude of the average material contrast depends strongly on the portion of the slow block being sampled. The differences in average slope likely indicate a combination of along-strike and downdip variation in the strength of the contrast. Additionally, the larger velocity contrast sensed by KEY than SUM for the same earthquakes indicates that head waves recorded close to the fault are sensitive to the material properties in the core of the FZ. Moreover, since KEY is about 700 m closer to the fault than SUM, the difference in the slopes of their moveout curves for the same region (.10 s km^{-1} versus .07 s km^{-1}) indicates that the differential times are sensitive to variations in elastic structure on shorter horizontal length scales than is achievable with direct wave traveltime tomography.

4.3 Head waveform modelling

The waveform shapes of FZHWs contain additional evidence for along-strike variations of fault properties and information on the detailed velocity structure of the FZ core. Fig. 7 compares the head waveforms recorded at SUM for events located to the SE and NW of the station. The events to the NW generate seismograms that are very similar to those expected for a simple planar interface between two elastic quarter spaces (Ben-Zion 1998, and Fig. 1). In particular, they begin with a near nodal head wave and almost no energy arrives between the head wave and the much larger direct wave. Fig. 9 shows synthetic waveform fits for vertical component displacement seismograms at station SUM generated by events in the relatively simple portion of the SAF to the NW of the station. The synthetic calculations are done with the 2-D analytical solution of Ben-Zion & Aki (1990) and Ben-Zion (1998) for the scalar wave equation in the plane-parallel layered FZ structure of Fig. 1 for a case with a single FZ layer. Motion is generated by an SH line dislocation with a unit step function in time. The solution assumes particle motion that is parallel to the structural interfaces and can thus be used to model fault-parallel and vertical component waveforms. The source is located at the interface between the fast quarter space and the FZ layer and the receiver is in the slower quarter space at a distance of 2.5 km from the FZ layer. Since the solution does not incorporate the full response to the *P*–*SV* system, it can be applied only up to the arrival of the direct wave, after which the seismograms become more complicated owing to *P*–*SV* conversions and *S*-wave energy trapped in the low-velocity damage zone. Obtaining a good fit to the data of Fig. 9 requires that we use different velocity models for the shallow ($Z = 3.8$ and 4.1 km) and deep ($Z = 6.9$ and 7.1 km) events, to account for the general increase in seismic velocities with depth in the crust. The resulting synthetic seismograms fit well the relative arrival times, amplitudes and motion polarities of the observed head and direct *P* waves.

The fit to the arrival times of the head and direct waves is more easily seen in velocity seismograms. Fig. 10 shows synthetic waveform fits for the early portions of two vertical-component velocity seismograms at station SUM generated by events to the NW of the station. The synthetic calculations do not provide a unique structural interpretation due to the large trade-offs between model parameters

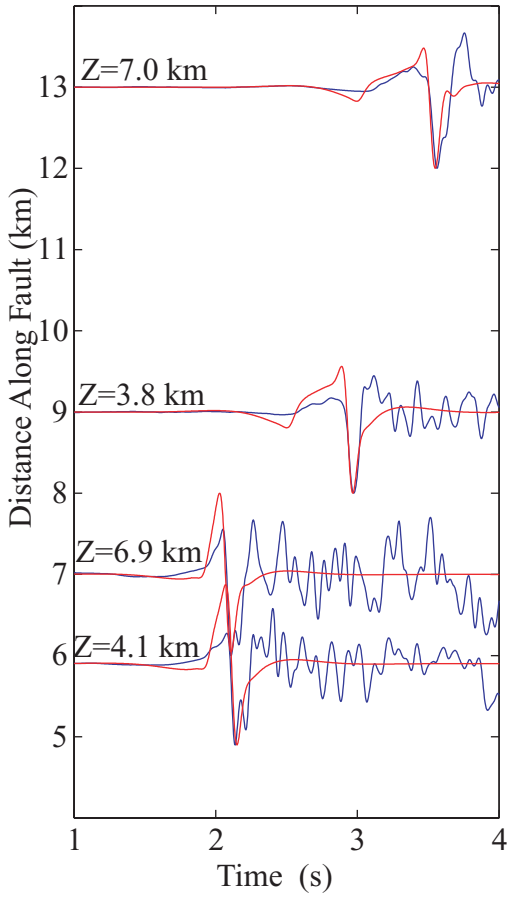

Figure 9. Synthetic fits (red) to displacement waveforms (blue) for four earthquakes located NW of station SUM in the relatively simple portion of the fault. Traces are plotted at *y* axis values corresponding to their distance traveled along the fault and labelled according to their source depth (Z). The synthetics were calculated for a simple fault model with a 100-m-thick damage zone between two quarter spaces. Different velocity models were used for the shallow ($Z \sim 4$ km) and deep ($Z \sim 7$ km) events to account for the strong depth dependence of velocity in this region. The quarter space velocities were 4.9 and 3.7 km s^{-1} for the deep events and 4.5 and 3.2 km s^{-1} for the shallow events. The FZ layer velocity was 3.0 km s^{-1} for all events. Both data and synthetic traces were filtered with a second-order butterworth filter with corner frequencies of 1 and 10 Hz. The receiver was positioned at 2.5 km normal distance from the fault on the slow (NE) side. The Q values were set at 200 outside and 20 inside the FZ.

(e.g. Ben-Zion 1998; Ben-Zion *et al.* 2003). Nevertheless, the results of Figs 9 and 10 indicate that an acceptable fit to the head and direct wave data generated by events to the NW of station SUM requires that the fault juxtapose two quarter spaces with significantly different elastic properties. In contrast to the head waveforms discussed above, arrivals from the SE of station SUM also begin with a near nodal head wave, but considerable energy arrives (Fig. 7 right) between the head and direct waves for earthquakes located at large offsets ($> \sim$10 km along the fault) to the SE of SUM. This energy has a moveout corresponding to a velocity slower than that of the first arriving head wave, but faster than the direct wave. Fig. 11 demonstrates that this energy first becomes visible at station KEY for earthquakes located sufficiently far to the SE to be within the two-strand region of the fault. Earthquakes located NW of this boundary, as defined by the earthquake relocations, generate relatively simple head waveforms, while those located just within this region show

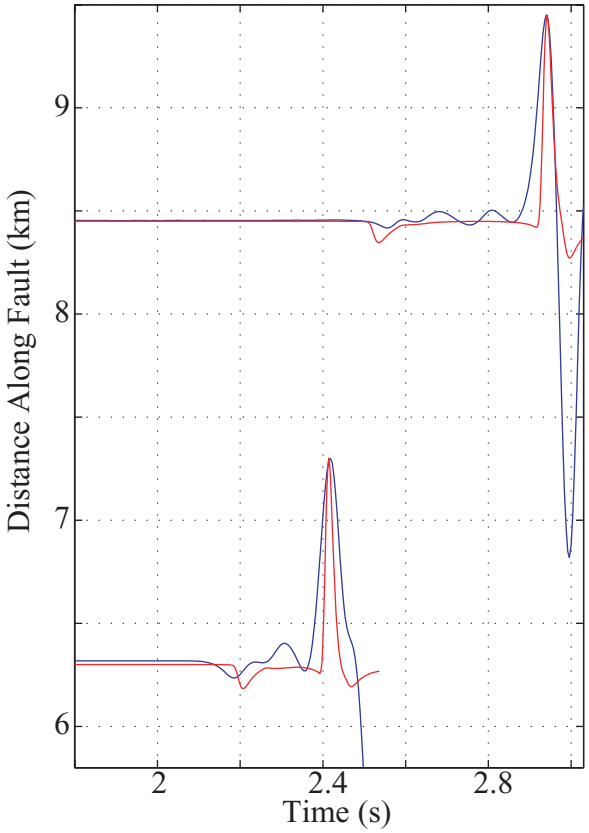

Figure 10. Examples of synthetic waveform fits (red) to observed velocity seismograms (blue) with a one-layer FZ model that separates two quarterspaces with different elastic properties. The observed seismograms were recorded at station SUM from two earthquakes located to the NW of the station. The waveforms show a low-amplitude head wave first arrival followed by an opposite polarity direct wave. The separation of the two arrivals increases with distance between the source and station. The synthetic waveforms are calculated using the solution of Ben-Zion & Aki (1990) and Ben-Zion (1998) for a 3-media version of the model in Fig. 1. The source is at the interface between media 1 and 2 and the assumed media properties are $c_1 = 6.0\,\mathrm{km\,s^{-1}}$ $c_2 = 2.5\,\mathrm{km\,s^{-1}}$, $c_3 = 3.25\,\mathrm{km\,s^{-1}}$, $Q_1 = 100$, $Q_2 = 100$, $Q_3 = 100$, $W_2 = 85$ m. The receiver was located 4.2 km normal to the fault on the slow side.

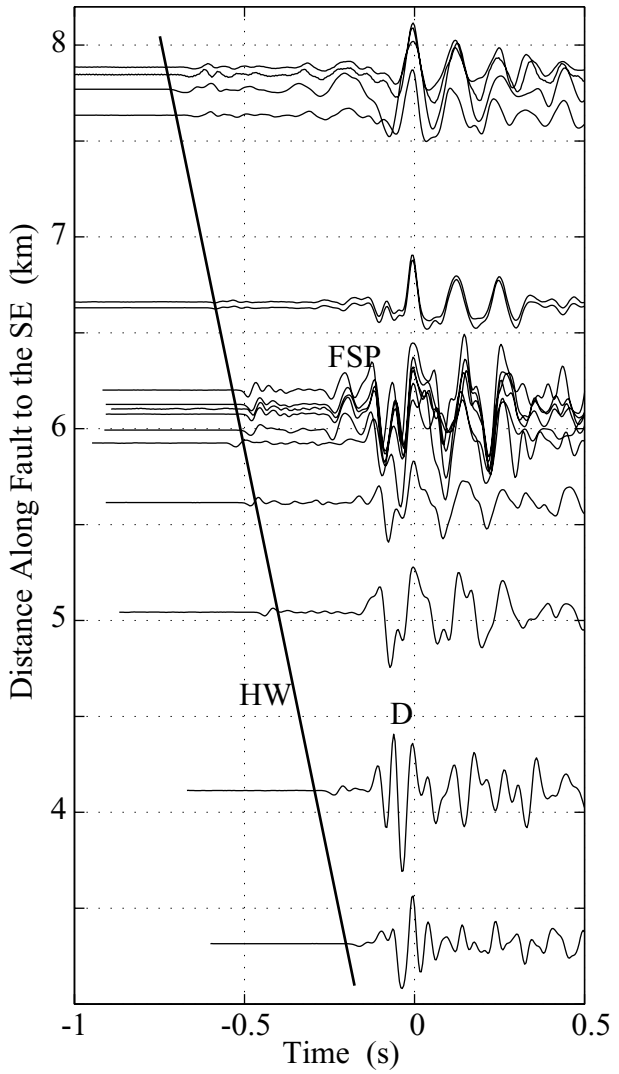

Figure 11. Observed *P* waveforms recorded at station KEY. Earthquakes in the two-strand region of the SAF (distances >6 km) produce more complicated head waveforms with evidence for a Fast Sliver Phase (labelled FSP), similar to that seen at station SUM.

large amplitude arrivals between the head and direct waves similar to those seen at SUM.

The considerable energy in the time interval between the head and direct waves for events to the SE of stations SUM and KEY is not produced in simple FZ structures such as a fault that directly juxtaposes two quarter spaces with different elastic properties, or a structure that contains a low-velocity core in-between two different quarter spaces (Figs 9 and 10). Instead, the observed energy between the head and direct waves indicates the presence of a wave-guide within the FZ with a velocity intermediate to that of the two surrounding crustal blocks. Fig. 12 shows examples of waveforms generated by a 3-media structural model, with the middle FZ layer having a velocity intermediate to those of the two surrounding quarter spaces. In this simple model, the intermediate velocity layer produces an arrival, labelled as the Fast Sliver Phase (FSP), whose amplitude and arrival time are controlled by the velocity, thickness, and Q value of the assumed layer. To demonstrate that the energy arriving between the head and direct waves for earthquakes located SE of SUM is consistent with an intermediate velocity layer, we produce a synthetic waveform fit to a typical vertical component seismogram, using the solution of Ben-Zion & Aki (1990) and Ben-Zion (1998) for a 4-media model (Fig. 13). The model represents the structure seen in the surface geology and seismicity relocations with a ∼500-m-thick sliver of granite between the fast and slow quarter spaces. There may also be a ∼100-m-thick shallow low-velocity FZ layer between the sliver and the slow quarter space. This is not required by the head waves but may be required by later portions of the *P* arrival and is consistent with previous active source studies (Li *et al.* 1997). The synthetic calculations provide again a reasonable fit for the relative arrival times, amplitudes and motion polarities of the main early phases. One quantitative result of our forward modelling is that to generate arrivals between the head and direct waves with amplitudes close to that of the direct wave, requires that the intermediate velocity layer have a significant thickness (>200 m) and/or a very high Q. If the intermediate velocity layer corresponds to the sliver of granite between the two fault strands, the amplitudes of the FSP arrivals in Figs 12 and 13 confirm the estimate of the sliver's thickness at seismogenic depths from earthquake relocations and extrapolation of the surface mapping.

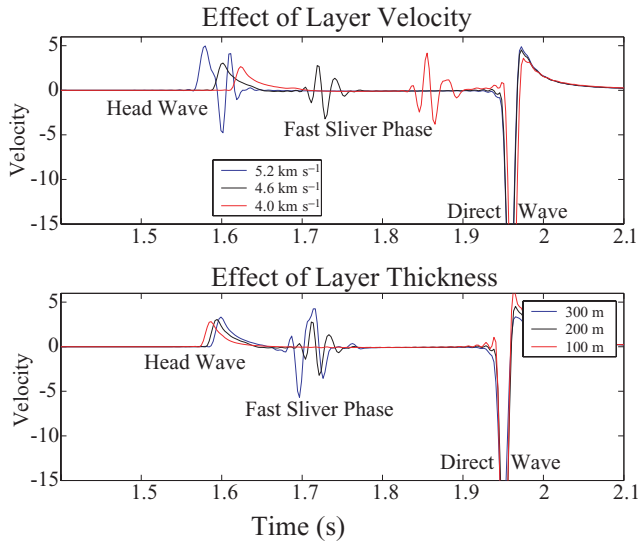

Figure 12. Examples of head waves and fast sliver phase, for the FZ model of Fig. 1 with $c_1 > c_2 > c_3 = c_4$. (Top) Velocity seismograms for three different values of c_2 at a station located about 1 km normal to the fault on the slow side. (Bottom) Velocity seismograms generated by three different thicknesses of the intermediate layer.

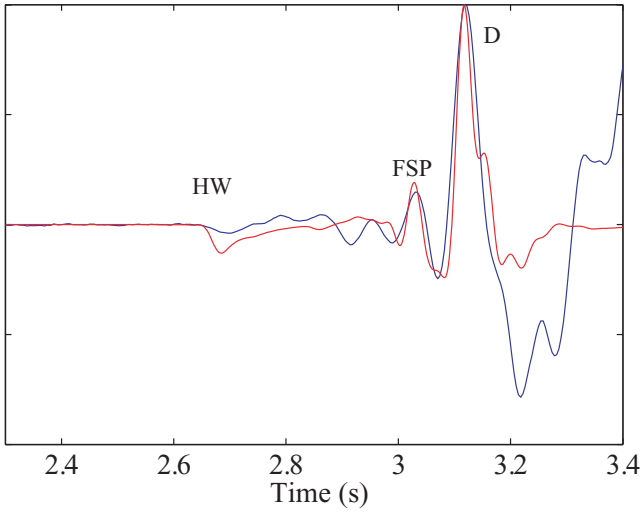

Figure 13. An example of a synthetic waveform fit with a 4-media model that includes a sliver of relatively fast material. The observed seismogram (blue) was recorded at station SUM from an earthquake located about 8 km to the SE at a depth of about 6.4 km. The synthetic waveform (red) is calculated using the solution of Ben-Zion & Aki (1990) and Ben-Zion (1998) for the model of Fig. 1. The source is at the interface between media 2 and 3 and the assumed media properties are $c_1 = 5.4\,\mathrm{km\,s^{-1}}, c_2 = 3.9\,\mathrm{km\,s^{-1}}, c_3 = 2.5\,\mathrm{km\,s^{-1}}, c_4 = 3.4\,\mathrm{km\,s^{-1}}$, $Q_1 = 300$, $Q_2 = 200$, $Q_3 = 200$, $Q_4 = 150$, $W_2 = 510$ m, and $W_3 = 93$ m. The receiver was located 2.5 km normal to the fault on the slow side. The head wave (H), Fast Sliver Phase (FSP) and Direct (D) arrivals are labelled on the seismograms. Many combinations of values for the wave-speed, thickness, and station offset parameters produce similar synthetic waveforms. However, the basic employed geometry, with a large velocity contrast between the two quarter spaces and an intermediate velocity (sliver) layer, is necessary to produce significant energy between the head and direct waves.

5 DISCUSSION

The structure of the SAF in the Bear Valley region has sharp material interfaces that are well documented in the surface geology. The head waveform data set employed in this study contains fundamental information that can be used to document the continuity and strength of the material interfaces in the seismogenic zone. Fig. 14 summarizes our results in map and cross-section views. The observation that the moveout of the head wave with respect to the direct wave increases with up-dip propagation distance (even for sources with negligible along-strike propagation) requires that the FZ material interface extends throughout the seismogenic zone. Our measurements of the increase in these differential traveltimes for different combinations of sources and receivers indicate systematic variations of the strength of the velocity contrast in the along-strike, fault-normal, and downdip directions. The larger velocity contrasts (∼50 per cent) required by the differential traveltime data at stations located close to the fault, as compared to further away (∼35 per cent) for the same earthquakes, indicates the presence of a very low-velocity damage zone, at least in the shallowest portion of the fault. The magnitude of the velocity reduction in the damage zone (>50 per cent) compares well with the results of Thurber *et al.* (1997) and Li *et al.* (1997). Detailed waveform modelling will be required to determine the depth extent of this damage zone. The combination of precise relocations and the waveform character in the time period between the head and direct wave arrivals can reveal sub-km-scale information about the subsurface structure of the FZ. The results indicate that some elements of the FZ structure observed at the surface (i.e. overall velocity contrast across the fault and localized sliver of granite) extend to the seismogenic zone. More complete traveltime and waveform inversions of head and direct *P* waves will be needed to fully utilize these data for creating detailed 3-D high-resolution images of the FZ properties that go beyond the overall characterization of Fig. 14. The sensitivity to short wavelength structure at seismogenic depths indicates that head waves may be a powerful monitoring tool for detecting changes in the material properties of the FZ over the course of the earthquake cycle.

The extension of a sharp material interface throughout the seismogenic zone in the Bear Valley region presents an opportunity to test the hypothesis that such an interface will induce a preference for rupture propagation to the SE. While our study area does not directly overlap with that of Rubin & Gillard (2000) and Rubin (2002), it probably has implications for their observations of an along-strike asymmetry in microearthquake aftershock locations. Our results indicate that, at least on short length scales (i.e. <2 km), the magnitude of the velocity contrast (20–50 per cent) is at the upper range of or larger than what has typically been used in numerical and laboratory studies. We also find that the velocity of the material on the NE side of the fault shows considerable along-strike, down dip and fault-normal variations. Moreover, at least some of the deeper earthquakes may be occurring on a granite-granite interface rather than a granite–sediment interface. Thus, seismicity in some locations may be expected to show more evidence of the aftershock asymmetry than others. Additionally, even in the case of this unusually large velocity contrast, there appears to be a low-velocity damage zone in the FZ core (width <1 km) although its depth extent is not yet constrained. Thus, the smallest earthquakes may not 'sense' the overall velocity contrast across the SAF if they ruptured a surface within this zone. These factors may contribute to the relatively small portion of mainshocks that produced the observed aftershock asymmetry in Rubin & Gillard (2000).

McGuire (2004) preformed direct inversions for the rupture directivity in two magnitude ∼2.7 earthquakes recorded by the temporary PASSCAL array. Both were shallow events in the region to the SE of station SUM, indicating that they likely ruptured on the

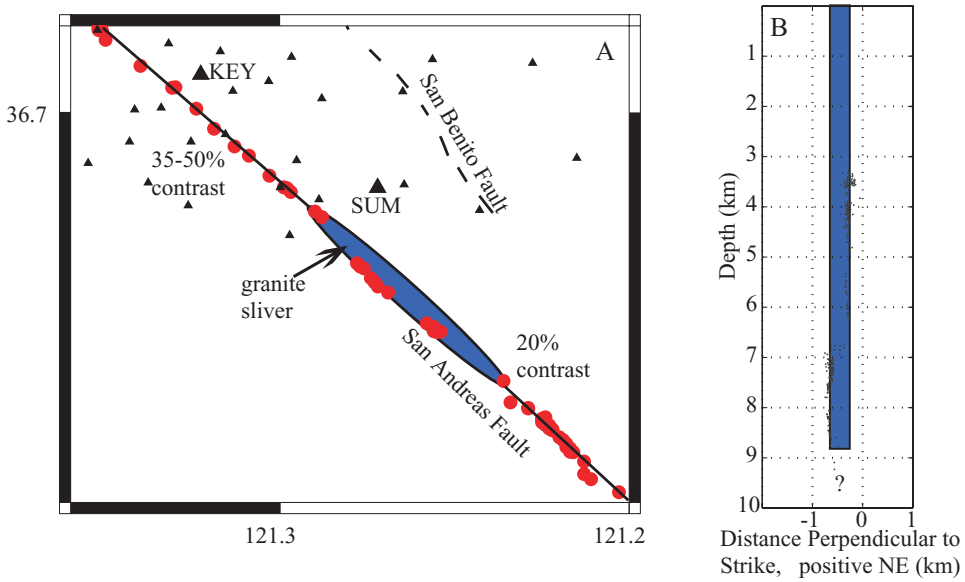

Figure 14. Schematic summary of the results from the waveform and traveltime analysis of head waves at SUM and KEY. (A) Map view of the San Andreas Fault (black lines), seismic stations (black triangles), and earthquakes (red circles) that generated the head-waves used in Figs 4, 6, 7, 9–11, 13. The inferred granite sliver is shown in blue to approximately correspond to the map of Dibblee (1974). The areas southeast (20 per cent) and northwest (35–50 per cent) of SUM are labelled with their estimated velocity contrasts. The 20 per cent and 35 per cent values reflect contrasts between the bounding crust blocks, while the 50 per cent values includes a contribution from the damaged FZ layer. (B) Cross-section view of the area immediately southeast of station SUM showing the granite sliver (blue) and the relative earthquake relocations (black dots) that define the two fault strands shown in Fig. 5.

granite–sediment interface (or possibly within a lower velocity damage zone associated with this FZ). One of these events showed clear unilateral rupture propagation to the SE (as predicted by the overall material contrast across the SAF), while the other was roughly bilateral. An imaging study of rupture properties associated with a considerably larger data set is required to test the theoretical prediction of a preferred propagation direction along a material interface. The wrinkle-like rupture is a pure mode II phenomenon involving rupture propagation in the direction that is parallel to the particle motion (e.g. Weertman 1980; Adams 1995; Ben-Zion 2001). Small strike-slip earthquakes expanding in two directions on the SAF are in general a mixture of modes II and III ruptures. However, as such earthquakes grow they are expected to become increasingly more mode II ruptures. In particular, moderate and large earthquakes on strike-slip faults that saturate the seismogenic zone will be predominantly mode II ruptures. Thus a detailed testing of predictions of the wrinkle-like rupture model requires imaging rupture properties of events that are large enough to have a significant Mode II component, but small enough to obtain in a few years a sufficient data set needed for statistical significance. Earthquakes larger than about M3.5 may provide a proper compromise between these two conflicting requirements for event size.

ACKNOWLEDGMENTS

We thank the IRIS DMC for distributing the Bear Valley data set and Cliff Thurber for answering various questions about it. JM was supported by the Hoch Fund for innovative research. The manuscript benefited from detailed constructive reviews by two anonymous referees and associate editor G. Laske.

REFERENCES

Adams, G., 1995. Self-excited oscillations of two elastic half-spaces sliding with a constant coefficient of friction, *J. Appl. Mech.,* **62,** 867–872.

Aki, K. & Lee, W.H.K., 1976. Determination of three-dimensional velocity anomalies under a seismic array using fist P arrival times from local earthquakes, I, a homogeneous initial model, *J. geohys. Res.,* **81,** 4381–4399.

Andrews, D. & Ben-Zion, Y., 1997. Wrinkle-like slip pulse on a fault between different materials, *J. geohys. Res.,* **102,** 553–571.

Anooshehpoor, A. & Brune, J.N., 1999. Wrinkle-like Weertman pulse at the interface between two blocks of foam rubber with different velocities, *Geophys. Res. Let.,* **23,** 2025–2028.

Bakun, W.H., Stewart, R.M., Bufe, C.G. & Marks, S.M., 1980. Implications of seismicity for failure of a section of the San Andreas fault, *Bull. seism. Soc. Am.,* **70,** 185–201.

Ben-Zion, Y., 1989. The response of two joined quarter spaces to SH line sources located at the material discontinuity interface, *Geophys. J. Int.,* **98,** 213–222.

Ben-Zion, Y., 1990. The response of two half spaces to point dislocations at the material interface, *Geophys. J. Int.,* **101,** 507–528.

Ben-Zion, Y., 1998. Properties of seismic fault zone waves and their utility for imaging low-velocity structures, *J. geohys. Res.,* **103,** 12 567–12 585.

Ben-Zion, Y., 2001. Dynamic ruptures in recent models of earthquake faults, *J. Mech. Phys. Solids,* **49,** 2209–2244.

Ben-Zion, Y. & Aki, K., 1990. Seismic radiation from an SH line source in a laterally heterogeneous planar fault zone, *Bull. seism. Soc. Am.,* **80,** 971–994.

Ben-Zion, Y. & Andrews, D.J., 1998. Properties and implications of dynamic rupture along a material interface, *Bull. seism, Soc. Am.,* **88,** 1085–1094.

Ben-Zion, Y. & Huang, Y., 2002. Dynamic rupture on an interface between a compliant fault zone layer and a stiffer surrounding solid, *J. Geophys. Res.,* **107,** doi: 10.1029/2001JB000254.

Ben-Zion, Y., Katz, S. & Leary, P., 1992. Joint inversion of fault zone head waves and direct P arrivals for crustal structure near major faults, *J. geophys. Res.,* **97,** 1943–1951.

Ben-Zion, Y. & Malin, P., 1991. San Andreas fault zone head waves near Parkfield California, *Science,* **251,** 1592.

Ben-Zion, Y. *et al.*, 2003. A shallow fault zone structure illuminated by trapped waves in the Karadere-Duzce branch of the North Anatolian Fault, western Turkey, *Geophys. J. Int.,* **152,** 699–717.

Blanpied, M.L, Lockner, D.A. & Byerleee, J.D., 1992. An earthquake mechanism based on rapid sealing of faults, *Nature,* **359,** 574–576.

Chester, F.M. & Chester, J.S., 1998. Ultracataclasite structure and friction processes of the Punchbowl fault, San Andreas system, California, *Tectonophysics,* **295,** 199–221.

Cochard, A. & Rice, J., 2000. Fault rupture between dissimilar materials: Ill-posedness, regularization, and slip-pulse response, *J. geophys. Res.,* **105,** 25 891–25 907.

Dibblee, T.W., 1974. *Geologic map of the Salinas quadrangle,* California, in Open-file report 74–1021, U.S. Geological Survey.

Dieterich, J.H., 1979. Modeling of rock friction 1. Experimental results and constitutive equations, *J. geophys. Res.,* **84,** 2161–2168.

Eberhart-Phillips, D. & Michael, A.J., 1993. Three-dimensional velocity structure, seismicity, and fault structure in the Parkfield Region, Central California, *J. geophys. Res.,* **98,** 15 737–15 758.

Eberhart-Phillips, D., Stanley, W.D., Rodriquez, B.D. & Lutter, W.J., 1995. Surface seismic and electrical methods to detect fluids related to faulting, *J. geophys. Res.,* **97,** 12 919–12 936.

Ellsworth, W., 1975. Bear Valley, California, earthquake sequence of February-March 1972, *Bull. seism. Soc. Am.,* **65,** 483–506.

Evans, J.P. & Chester, F.M., 1995. Fluid-rock interaction in faults of the San Andreas system: inferences from SanGabriel fault rock geochemistry and microstructures, *J. geophys. Res.,* **100,** 13 007–13 020.

Fialko, Y., Sandwell, D., Agnew, D., Simons, M., Shearer, P. & Minster, B., 2002. Deformation on nearby faults induced by the 1999 Hector Mine earthquake, *Science,* **297,** 1858–1862.

Fohrmann, M., Igel, H., Jahnke, G. & Ben-Zion, Y., 2004. Guided waves from sources outside faults: an indication for shallow fault zone structure?, *Pure appl. Geophys.,* **161,** 2125–2137.

Fuis, G.S., Rybers, T., Lutter, W.J. & Ehlig, P.L., 2001. Seismic mapping of shallow fault zones in the San Gabriel Mountains from the Los Angeles region seismic experiment, Southern California, *J. geophys. Res.,* **106,** 6549–6568.

Haberland, C. *et al.*, 2003. Modeling of seismic guided waves at the Dead Sea transform, *J. geophys. Res.,* **108**(B7), 2342, doi:10.1029/2002JB002309.

Hough, S.E., Ben-Zion, Y. & Leary, P., 1994. Fault zone waves observed at the southern Joshua Tree earthquake rupture zone, *Bull. seism. Soc. Am.,* **84,** 761–767.

Igel, H., Jahnke, G. & Ben-Zion, Y., 2002. Numerical simulation of fault zone guided waves: accuracy and 3-D effects, *Pure appl. Geophys.,* **159,** 2067–2083.

Jahnke, G., Igel, H. & Ben-Zion, Y., 2002. Three-dimensional calculations of fault zone guided wave in various irregular structures, *Geophys. J. Int.,* **151,** 416–426.

Johnson, A.M., Fleming, R.W., Cruikshank, K.M., Martosudamo, S.Y., Johnson, N.A. & Johnson, K.M., 1997. Analecta of structures formed during the 28 June 1992 Landers-Big Bear California earthquake sequence, *U.S. Geol. Surv. Open File Rep.,* **97–94**, 59.

Korneev, V.A., Nadeau, R.M. & McEvilly, T.V., 2003. Seismological studies at Parkfield IX: fault-zone imaging using guided wave attenuation, *Bull. seism. Soc. Am.,* **93,** 1415–1426.

Lees, J.M. & Malin, P.E., 1990. Tomographic Images of P wave velocity variation at Parkfield California, *J. geophys. Res.,* **95,** 21 793–21 804.

Lewis, M.A, Peng, Z., Ben-Zion, Y. & Vernon, F., 2005. Shallow seismic trapping structure in the San Jacinto fault zone, *Geophys. J. Int.,* **162,** 867–881.

Li, Y.-G., Ellsworth, W., Thurber, C., Malin, P. & Aki, K., 1997. Fault-zone guided waves from explosions in the San Andreas fault in Parkfield and Cienega Valley California, *Bull. seism. Soc. Am.,* **87,** 210–221.

Li, Y.G. & Leary, P.C., 1990. Fault zone trapped seismic waves, *Bull. seism. Soc. Am.,* **80,** 1245–1274.

Li, Y.G., Aki, K., Adams, D., Hasemi, A. & Lee, W.H.K., 1994a. Seismic guided waves trapped in the fault zone of the Landers, California earthuqake of 1992, *J. geophys. Res.,* **99,** 11 705–11 722.

Li, Y.G., Vidale, J.E., Aki, K., Marone, C.J. & Lee, W.H.K., 1994b. Fine structure of the Landers fault zone: segmentation and the rupture process, *Science,* **256,** 367–370.

Li, Y.G., Vidale, J.E., Aki, K., Xu, F. & Burdette, T., 1998. Evidence of shallow fault zone strengthening after the 1992 M 7.5 Landers, California, Earthquake, *Science,* **279,** 217–219.

Lyakhovsky, V., Ben-Zion, Y. & Agnon, A., 2001. Earthquake cycle, fault zones, and seismicity patterns in a rheologically layered lithosphere, *J. geophys. Res.,* **106,** 4103–4120.

Mamada, Y., Kuwahara, Y., Ito, H. & Takenaka, H., 2004. Discontinuity of the Mozumi-Sukenobu fault low-velocity zone, central Japan, inferred from 3-D finite-difference simulations of fault zone waves excited by explosive sources, *Tectonophysics,* **378,** 209–222.

Marone, C., 1998. Laboratory-derived friction laws and their application to seismic faulting, *Annu. Rev. Earth Planet. Sci.,* **26,** 643–649.

Marone, C., Vidale, J.E. & Ellsworth, W.L., 1995. Fault healing inferred from time dependent variations in source properties of repeating earthquakes, *Geophys. Res. Lett.,* **22,** 3095–3098.

Massonnet, D.W.T. & Vadon, H., 1996. Detection of fault-zone collapse following the Landers earthquake, *Nature,* **382,** 612–616.

McGuire, J.J., 2004. Estimating the finite source properties of small earthquake ruptures, *Bull. seism. Soc. Am.,* **94,** 377–393.

McNally, K.C. & McEvilly, T.V., 1977. Velocity contrast across the San Andreas Fault in central California, small-scale variations from P-wave nodal plane distortion, *Bull. seism. Soc. Am.,* **67,** 1565–1576.

Michael, A. & Ben-Zion, Y., 1998. Inverting fault zone trapped waves with a genetic algorithm, *EOS, Trans. Am. geophys. Un.,* **79,** F584.

Michelini, A. & McEvilly, T.V., 1991. Seismological studies at Parkfield: I. Simultaneous inversion for velocity structure and hypocenters using B-splines parameterization, *Bull. seism. Soc. Am.,* **81,** 524–552.

Nishigami, K., Ando, M. & Tadokoro, K., 2001. Seismic observations in the DPRI 1800 m borehole drilled into the Nojima fault zone, south-west Japan, *Island Arc,* **10,** 288–295.

Paige, C.C. & Saunders, M.A., 1982. LSQR: Sparse linear equations and least squares problems, *ACM Transactions on Mathematical Software,* **8**(2), 195–209.

Peng, Z., Ben-Zion, Y., Michael, A.J. & Zhu, L., 2003. Quantitative analysis of seismic trapped waves in the rupture zone of the 1992 Landers, California earthquake: Evidence for a shallow trapping structure, *Geophys. J. Int.,* **155,** 1021–1041.

Ranjith, K. & Rice, J., 2001. Slip dynamics at an interface between dissimilar materials, *J. Mech. Phys. Solids,* **49,** 341–361.

Rovelli, A., Caserta, A., Marra, F. & Ruggiero, V., 2002. Can seismic waves be trapped inside an inactive fault zone? The case study of Nocera Umbra, central Italy, *Bull. seism. Soc. Am.,* **92,** 2217–2232.

Rubin, A., 2002. Aftershocks of microearthquakes as probes of the mechanics of rupture, *J. geophys. Res.,* **107,** doi:10.1029/2001JB0000496.

Rubin, A. & Gillard, D., 2000. Aftershock asymmetry/rupture directivity along central San Andreas fault microearthquakes, *J. geophys. Res.,* **105,** 19 095–19 109.

Schaff, D.P., Bokelmann, G.H.R., Beroza, G.C., Waldhauser, F. & Ellsworth, W.L., 2002. High resolution image of Calaveras Fault seismicity, *J. geohys. Res.,* **107**(9), doi: 10.1029/2001JB 000633.

Schallamach, A., 1971. How does rubber slide, *Wear,* **17,** 301–312.

Scholz, C.H., 2002. *The Mechanics of Earthquake Faulting,* Cambridge Univ. Press, Cambridge.

Sibson, R.H., 1977. Fault rocks and fault mechanisms, *J. geol. Soc. London,* **133,** 191–213.

Stewart, S.W., 1968. Preliminary comparison of seismic travel times and inferred crustal structure adjacent to the San Andreas fault in the Diablo and Gabilan ranges of central California, *Stanford University Publications, Geological Sciences,* **11,** 218–230.

Stierman, D.J., 1984. Geophysical and geological evidence for fracturing, water circulation, and chemical alteration in granitic rocks adjacent to major strike-slip faults, *J. geohys. Res.,* **89,** 5849–5857.

Tanimoto, T. & Sheldrake, K.P., 2002. Three-dimensional *S*-wave velocity structure in Southern California, *Geophys. Res. Lett.,* **29,** doi: 10.1029/2001GL013486.

Thurber, C., Roecker, S., Ellsworth, W., Chen, Y., Lutter, W. & Sessions, R., 1997. Two-dimensional seismic image of the San Andreas Fault in the

Northern Gabilan Range, central California: Evidence for fluids in the fault zone, *Geophys. Res..Lett.,* **24,** 1591–1594.

Waldhauser, F. & Ellsworth, W., 2000. A double-difference earthquake location algorithm: method and application to the northern Hayward Fault, *Bull. seism. Soc. Am.,* **90,** 1330–1368.

Walter, A.W. & Mooney, W.D., 1982. Crustal structure of the Diablo and Gabilain ranges central California; a reinterpretation of existing data, *Bull. seism. Soc. Am.,* **72,** 1567–1590.

Weertman, J., 1980. Unstable slippage across a fault that separates elastic media of different elastic constants, *J. geophys. Res.,* **85,** 1455–1461.